nature communications

Article

https://doi.org/10.1038/s41467-025-58473-3

Predeposited lead nucleation sites enable a highly reversible zinc electrode for stable zinc-bromine flow batteries

Received: 11 September 2024

Accepted: 24 March 2025

Published online: 05 April 2025

Check for updates

Yichan Hu[1,2,7], Zhiwen Min[2,3,4,7], Guangyu Zhu[2], Yuanwei Zhang[3], Yixian Pei[3], Cong Chen[5], Yuanmiao Sun[2,3] ✉, Guojin Liang[2,3] ✉ & Hui-Ming Cheng[2,3,6]

Aqueous zinc-bromine flow batteries are promising for grid storage due to their inherent safety, cost-effectiveness, and high energy density. However, they have a low energy/power density and inferior cycle stability due to irreversible reactions of uncontrolled zinc dendrite growth and hydrogen evolution reaction. Here, we develop a highly reversible carbon felt electrode with uniformly distributed Pb nanoparticles, which can be realized via an effective in situ predeposition strategy. Owing to abundant Pb nanoparticles as zincophilic nucleation sites, the Pb nanoparticles effectively induce uniform Zn deposition with a dendrite-free morphology. Moreover, the Pb-modified electrode accommodates higher hydrogen evolution reaction overpotential to inhibit the H_2 evolution. Consequently, the modified electrode-based zinc-bromine flow batteries demonstrate a cumulative plating capacity (23 Ah cm^{-2}) over 2300 h with an average Coulombic efficiency of over 97.4%. This work contributes insights into the design of highly reversible Zn electrode in Zn-based flow batteries.

Large-scale energy storage technologies are essential for addressing the inherent intermittency and volatility of renewable energy sources such as solar and wind[1–4]. Flow batteries (FBs) have emerged as promising candidates, notable for their design flexibility, well scalability, and decoupling of power from energy[5–7]. Aqueous Zn bromine flow batteries (ZBFBs) draw particular attention due to their inherent safety, environmental benefits, high energy density, and cost-effectiveness[8–12]. However, two primary irreversible reaction issues at the Zn negative electrode in ZBFBs, namely dendrite growth and hydrogen evolution reaction (HER), significantly deteriorate the Coulombic efficiency (CE) and cycle stability of ZBFBs. Furthermore, these challenging issues would be intensified under high operational areal capacity and current densities, constraining their performance in high-energy and high-power applications of ZBFBs[13–16].

Modifying the Zn deposition process to achieve uniform Zn deposition and suppressing hydrogen evolution is crucial for the long cycle life and high energy of ZBFBs. Various improvement strategies have been proposed to increase the reversibility of Zn negative electrodes in Zn-based FB systems, especially by modifying electrolytes, membranes, and electrodes[17–22]. Regarding the electrolyte modification, organic additives are usually used at the expense of increased voltage polarization[17–19]. On the other side, although designing new-type membranes, such as boron nitride composite membranes[20] and negatively charged membranes[21], could extend the battery cycle life by

[1]School of Materials Science and Engineering, Hunan University, Changsha 410000, China. [2]Faculty of Materials Science and Energy Engineering, Shenzhen University of Advanced Technology, Shenzhen 518055, China. [3]Institute of Technology for Carbon Neutrality, Shenzhen Institute of Advanced Technology, Chinese Academy of Sciences, Shenzhen 518055, China. [4]Institute of Applied Physics and Materials Engineering, University of Macau, Macau 999078, China. [5]School of Chemistry and Materials Science, Qinghai Minzu University, Xining 810007, China. [6]Shenyang National Laboratory for Materials Science, Institute of Metal Research, Chinese Academy of Sciences, Shenyang 110016, China. [7]These authors contributed equally: Yichan Hu, Zhiwen Min.
✉e-mail: sunym@siat.ac.cn; gj.liang@siat.ac.cn

preventing dendrites to puncture the membranes, it is still challenging to guide even Zn growth morphology on the current collector. To further improve the reversibility of the Zn negative electrode in a FB system, modification strategies on current collectors, e.g., the widely used carbon felt (CF), have been developed to achieve dendrite-free morphologies of the Zn negative electrode. For instance, specific metals, such as tin, titanium, and silver, have been deposited on CF electrodes by magnetron sputtering technology[22]. The as-obtained composite CF electrodes provide more Zn nucleation sites and higher HER overpotential than pure CF electrodes, which can effectively boost the Zn uniform deposition and suppress the H_2 evolution. However, they exhibited limited improvements in battery cycling lifetime compared to the control sample. Besides, such methods require specialized magnetron sputtering equipment, which is costly and time-consuming for large-scale preparation. Therefore, constructing a high-quality CF electrode in a cost-effective and facile way to realize a reversible Zn negative electrode is highly desired.

Regarding the performance evaluation in Zn-based batteries, a cumulative plating capacity (CPC) can serve as one significant parameter to quantify the total Zn deposited and stripped over cycles[5,23], where a higher CPC signifies greater cycle stability and reversibility for high-energy and consistent energy storage. Unfortunately, according to the previous reports, ZBFBs exhibit a generally low CPC (most below 10 Ah cm^{-2}, Supplementary Table 1) due to the irreversible Zn dendrites and the competing HER at the Zn negative electrode side. In aqueous zinc-based batteries, depositing hetero-metals (e.g., lead, tin, bismuth, and indium) on Zn electrodes/current collectors, often via displacement reactions or other deposition techniques, has been identified as an effective strategy to achieve reversible Zn negative electrode in Zn-ion battery systems. Specifically, the in situ predeposited zincophilic metals can promote a uniform morphology of the Zn negative electrode by providing sufficient Zn nucleation sites to reduce nucleation energy barriers and accelerate Zn deposition kinetics[24]. Moreover, it can effectively mitigate H_2 evolution by modifying the electrode interface with metal nanoparticles of higher HER overpotentials[25,26]. Among these metals, lead (Pb) has great potential for reversible Zn negative electrode due to its good corrosion resistance, capability to inhibit HER, and inherent zincophilicity[27,28]. Meanwhile, due to the higher oxidation potentials of heterometals compared to zinc, these heterometals can be stably retained on the zinc negative electrode after electrodeposition. Nevertheless, it should be noted that these strategies have been applied to Zn foil negative electrodes in Zn-ion battery systems, where their effectiveness and regulating mechanisms to suppress dendrite growth and H_2 evolution remain rarely explored for widely applied three-dimensional CF electrodes in flow battery systems.

Here, we develop a highly reversible Zn electrode with Pb nanoparticles uniformly distributed on CF (Pb@CF) for ZBFBs. The composite electrode surface is modified with Pb nanoparticles via a facile in situ electrodeposition strategy. The abundant Pb nanoparticles take a role as zincophilic nucleation sites to effectively anchor Zn atoms. It is found that the uniform Zn nucleation is facilitated for subsequent dendrite-free Zn deposition. Meanwhile, the high HER overpotential of Pb@CF electrodes effectively inhibits the competing HER. As a result, the Pb@CF-based FB system shows improved cycle stability and delivers higher CPC than the CF-based FB system. This study showcases the Pb@CF electrode as a cost-effective and efficient solution for improving the reversibility of Zn negative electrodes, substantially boosting the practical viability of ZBFBs for large-scale and low-cost energy storage applications.

Results

Working principle of Pb@CF composite electrodes

An in situ electrodeposition process is developed to obtain Pb@CF composite electrodes, where an unmodified electrode is denoted as CF and the electrode containing Pb nanoparticles is denoted as Pb@CF. Specifically, in a baseline electrolyte containing trace Pb^{2+} (1 mM, see Methods), a distinctive reduction peak at approximately −0.5 V versus an Ag/AgCl reference electrode is observed when scanned from 0 V to −0.65 V (Fig. 1a), which can be assigned to the reduction of Pb^{2+} due to the Zn^{2+} reduction potential is not triggered. Further analysis confirmed that the Pb^{2+} is predeposited at −0.5 V while Zn deposition occurred at −1.2 V versus an Ag/AgCl reference electrode within the same electrolyte (orange line in Fig. 1b). The deposits at these two different working potentials are confirmed by X-ray diffraction (XRD) (Fig. 1c). Meanwhile, the reduction potential of Zn^{2+} is shifted to a more positive potential for the Pb@CF electrode as −0.971 V compared to the CF electrodes (−1.028 V) in a Pb-free electrolyte.

Uniform Pb nanoparticles are deposited on the CF at a constant potential of −0.65 V for 30 s to produce sufficient zincophilic nucleation sites (Fig. 1d, e), which facilitates uniform Zn deposition. And optimization of Pb^{2+} concentration reveals that Pb@CF prepared with 1 mM Pb^{2+} exhibits the more uniform morphology and effective corrosion resistance (Supplementary Figs. 1 and 2). Subsequently, the Zn deposition after 1 min at 20 mA cm^{-2} is examined on the Pb@CF electrodes. The scanning electron microscopy (SEM) and the corresponding elemental mapping result show an evenly-sized Pb-Zn alloy morphology (Fig. 1f), due to predeposited Pb as the nucleation sites to guide the smooth growth of the Zn metal. It is reported that the initial morphology of Zn deposits predominantly depends on the number and distribution of nucleation sites on the electrode[29]. The Pb@CF electrode with abundant zincophilic nucleation sites leads to uniform Zn growth morphology. In contrast, Zn^{2+} randomly nucleated on the control CF due to the limited and disordered nucleation sites, and these sparse Zn nuclei grow to produce loose and unevenly sized Zn particles on the bare CF electrode, which leads to dendrite growth (Supplementary Fig. 3).

The morphology of Zn negative electrodes is used as a qualitative indicator of Zn deposition behaviors and the ongoing morphology of Zn deposition is assessed. At a constant test condition of 40 mA cm^{-2}, the result indicates that Pb nanoparticles can guide Zn growth, the Zn nuclei on the Pb@CF progressively merges into a compact Zn layer that fully encapsulates the electrode surface (Fig. 2a). Conversely, the control CF electrode exhibits sporadic and sparse nucleation, and Zn^{2+} continuously deposits on the existing nuclei to induce uneven growth (Fig. 2b). This unevenness stems from a limited and irregular distribution of nucleation sites to promote localized Zn deposition. Meanwhile, the Pb@CF electrode exhibits a compact and smooth zinc deposition morphology at various current densities (Supplementary Fig. 4), highlighting its high adaptability to current fluctuations compared to the CF electrode. Furthermore, even at an current density and areal capacity of 100 mAh cm^{-2}/100 mAh cm^{-2}, the Pb@CF electrode maintains a uniform and densely packed zinc layer (Supplementary Fig. 5), demonstrating its capability to effecively accommodate high-capacity operating conditions. Moreover, atomic force microscopy (AFM) is used to analyze the surface morphology of Zn deposits at 20 mA cm^{-2} for 20 min on a relatively flat 3D carbon paper (CP) substrate, where the CF is not applied here due to its highly rough three-dimensional structure with difficult in accurately measuring the surface flatness. It exhibits an smooth Zn surface with a low roughness ($R_a \approx 96.9$ nm) on the Pb@CP electrode (Supplementary Fig. 6). In contrast, the control CP electrode displays a rough and fluctuating surface topology ($R_a \approx 309$ nm) (Supplementary Fig. 7). These AFM observation results are consistent with the SEM results, confirming that the Pb-nanoparticles could effectively enable the dendrite-free morphology of the deposited Zn.

Ex situ XRD analysis is conducted to further understand the Zn deposition/dissolution behavior on Pb@CF electrodes (Fig. 2c). The Pb (111) peak is ultimately preserved without notable changes throughout the Zn deposition/stripping process under a current density of

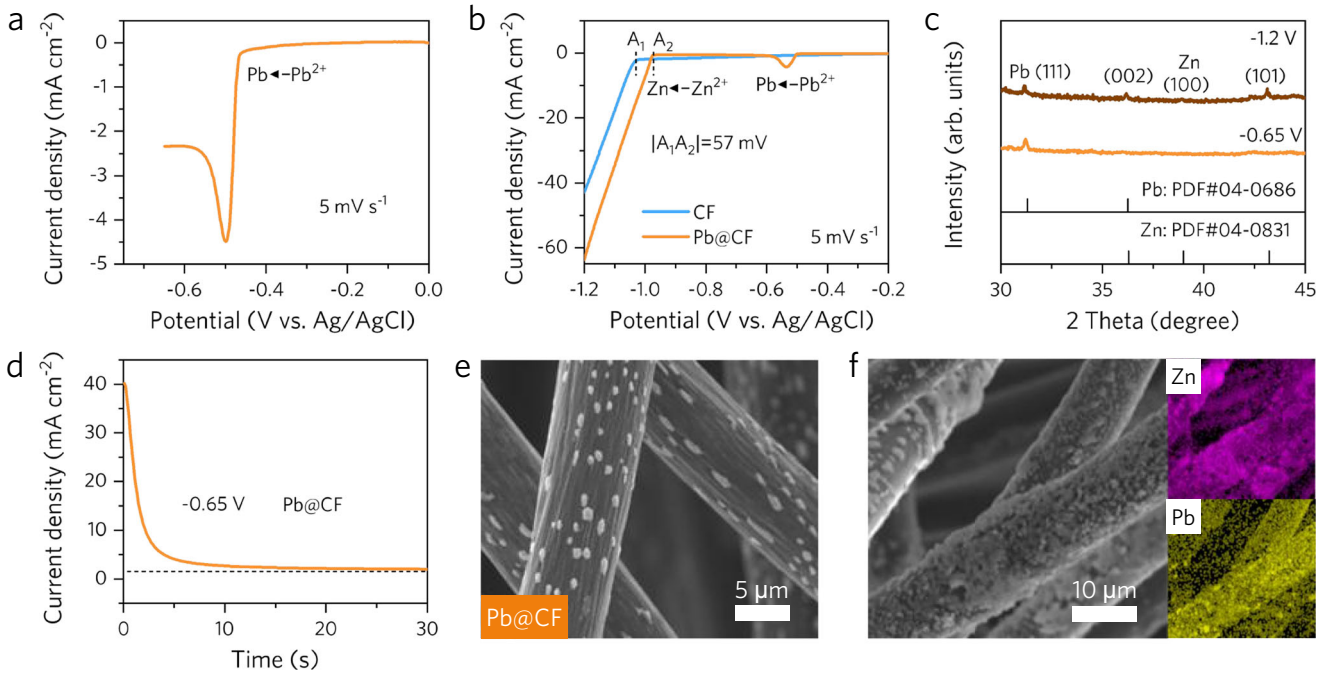

Fig. 1 | Fabrication and features of Pb@CF electrodes. a Voltage profile of electrochemical reduction of Pb^{2+}. **b** Voltage profiles of Zn^{2+} reduction on CF and Pb@CF electrodes. **c** XRD results corresponding to the deposits on CF and Pb@CF electrodes. **d** The I-t curve of the prepared Pb@CF electrode at a constant potential of -0.65 V, and **e** the corresponding SEM image of the Pb@CF electrode deposited at the potential of -0.65 V for 30 s versus the Ag/AgCl electrode. **f** The SEM image and corresponding elemental mappings deposited Zn metal on the Pb@CF electrode for 1 min at the potential of −1.2 V versus the Ag/AgCl electrode.

10 mA cm^{-2}, which implies the durability of the initially formed Pb atoms/clusters as Zn nucleation sites. Moreover, due to the different exposed areas of the used 3D CF electrode, glass carbon electrodes with the same area are used to characterize Zn nucleation and growth. Specifically, chronoamperometry results of Zn deposition under different potentials reveal the diffusion-controlled characteristics on both Pb-modified and control electrodes (Supplementary Fig. 8)[30]. The current-time results, i.e., the i-t data, are normalized to $(i/i_{max})^2$ versus (t/t_{max}) relationship and fitted with the Scharifer-Hills model (Fig. 2d and Supplementary Note 1), which implies that the Zn nucleation at the Pb-modified and control electrodes follows an instantaneous nucleation mode[30]. Therefore, the calculated nucleus density based on the transient current results of the instantaneous nucleation mode implies that the Pb-modified electrode provided higher nucleus density than the control electrode at different working potentials[31] (Fig. 2e and Supplementary Table 2), where the calculation process is elaborated in Supplementary Note 2. These results indicate a marked increase in the nucleation rate of Zn on the Pb-modified electrodes and support that the in situ predeposited Pb nanoparticles on Pb@CF electrodes provide more nucleation sites, facilitating uniform Zn nucleation during the initial Zn nucleation process. This uniform nucleation guides subsequent uniform Zn deposition for large deposition capacity.

Zn deposition kinetics based on a Pb@CF electrode

The Zn deposition kinetics is further investigated, where the Zn nucleation behaviors are closely related to the electrodeposition kinetics[29]. According to the classical nucleation theory, the nucleation of new solid phases requires overcoming the free energy barrier[32,33]. During Zn plating, the Gibbs energies of nucleation ($E_{nucleation}$) and growth (E_{growth}) correlates to the thermodynamic barriers for the formation of initial Zn nuclei and their subsequent expansion into larger deposits (Supplementary Fig. 9)[34]. Meanwhile, there is an energy difference between nucleation and growth, and the energy of growth is lower than that of nucleation. This is because it is thermodynamically more favorable to add zinc atoms to existing nuclei than to re-form stable clusters[35,36]. Higher energy differences result in subsequent Zn deposition preferentially on the existing Zn nuclei[34], which can induce non-uniform Zn sheets or dendrite structures on CF electrode. The Pb@CF electrode contributes to uniform Zn deposition by supplying numerous zincophilic nucleation sites, which can effectively decrease the difference (ΔE) between $E_{nucleation}$ and E_{growth}, i.e., $\Delta E_1 > \Delta E_2$ (Fig. 3a). The related energy of Zn deposition is electrochemically reflected as an overpotential in the voltage profile, which directly indicates the energy consumption during nucleation and growth, as it is proportional to the applied overpotential[37]. To verify it, the deposition voltage profiles at a constant current density are characterized, and the working voltage sharply drops and then rises during the Zn plating on the Pb@CF electrode (Fig. 3b and Supplementary Fig. 10). The nucleation overpotential (η_n) is the initial voltage drop of the nucleation process, representing the energy barrier necessary for critical cluster formation, while the overpotential (η_g) of a mass-transfer controlled process is correlated to the Zn growth process[26]. Specifically, the Pb@CF electrode presents a notable reduction in both η_n (249.1 mV) and η_g (235.6 mV) compared with the control CF electrode (η_n and η_g are 320.9 mV and 264.3 mV, respectively) (Fig. 3c). The smaller overpotential difference (Δη) between η_n and η_g based on the Pb@CF electrode signifies the smaller energy difference between the $E_{nucleation}$ and E_{growth} of the Zn growth[38], thereby diminishing the nucleation driving force to facilitate more uniform Zn deposition.

For an in-depth analysis of deposition kinetics, the exchange current density associated with Zn deposition is calculated (Eq. 1)[39]:

$$i = i_0 \frac{\eta F}{2RT} \quad (1)$$

where i, i_0, R, T, η, and F represent the current density, exchange current density, gas constant, deposition temperature, total overpotential, and Faraday constant, respectively. Under this definition, a higher exchange current density indicates more efficient Zn deposition dynamics. The calculation details are given in Supplementary

https://doi.org/10.1038/s41467-025-58473-3

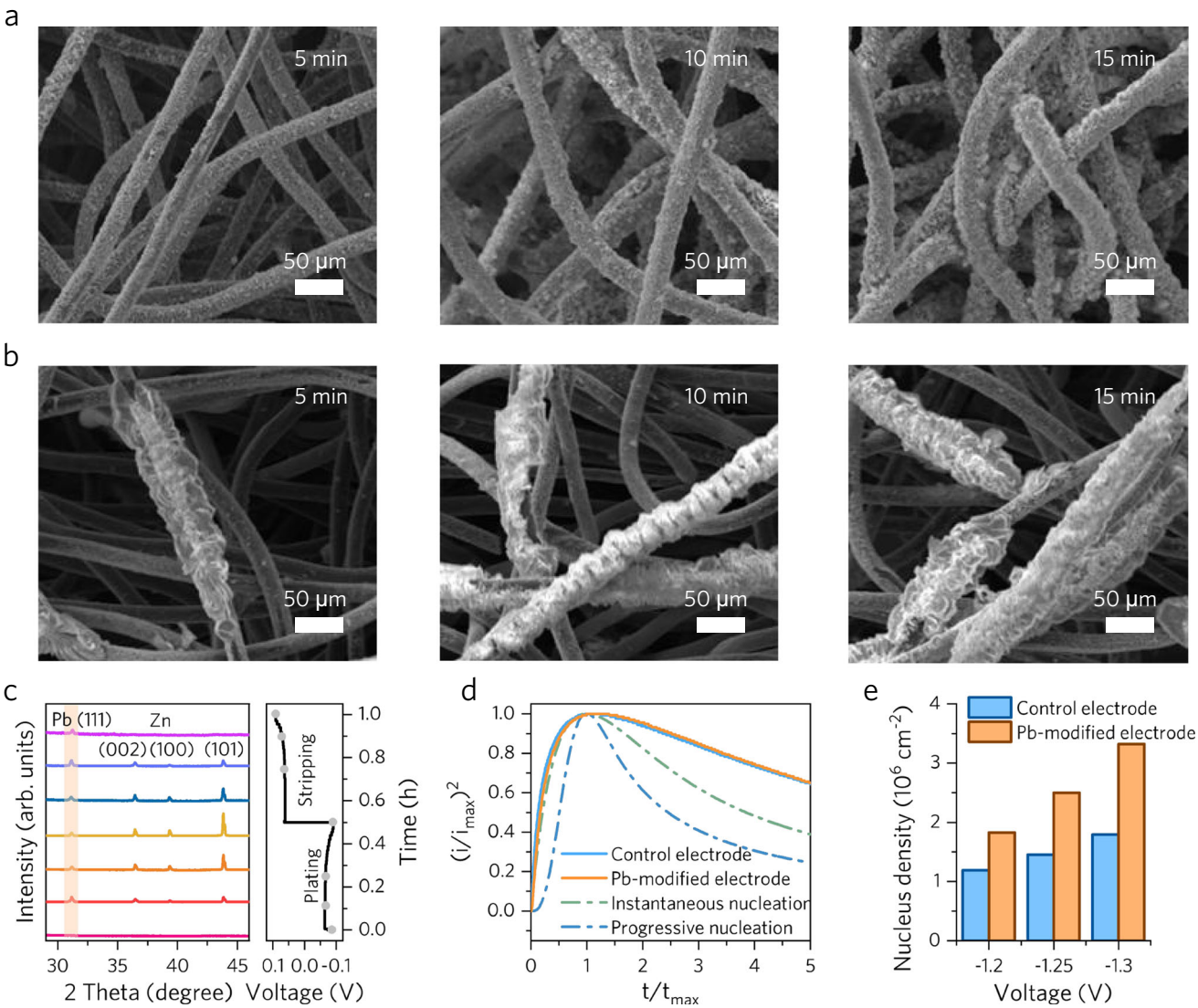

Fig. 2 | The Zn nucleation and growth behaviors. Deposited Zn morphologies on (**a**) Pb@CF and (**b**) CF electrodes at different deposition time and capacities under a current density of 40 mA cm^{-2}. **c** Ex situ XRD patterns of Zn plating/stripping on the Pb@CF electrode under a current density of 10 mA cm^{-2}. **d** Comparison of theoretical dimensionless plots for instantaneous and progressive nucleation models with experimental results at -1.3 V versus an Ag/AgCl electrode. **e** Calculated nucleus density at different deposition voltages based on the control and Pb-modified electrodes.

Note 3, Supplementary Tables 3 and 4. The exchange current density for Pb@CF (20.72 mA cm^{-2}) is notably higher than that for CF (14.04 mA cm^{-2}) (Fig. 3d), which can be attributed to the substantially improved Zn deposition kinetics of the Pb@CF. Typically, Zn^{2+} desolvation is regarded as the pivotal step controlling the deposition rate of Zn, significantly impacting the reaction dynamics throughout the process. The desolvation energy of Zn^{2+} on Pb@CF is determined through Eq. (2)[40,41]:

$$\frac{1}{R_{ct}} = A \exp\left(\frac{-E_a}{RT}\right) \quad (2)$$

where R_{ct}, A, R, T, and E_a represent the charge transfer resistance, the constant, the gas constant, the Kelvin temperature, and the activation energy, respectively. The R_{ct} is correlated to the semicircles of the EIS profile within the high-frequency range (Supplementary Fig. 11). As a result, Pb@CF electrodes present a lower desolvation energy of 42.73 kJ mol^{-1} than that of the CF electrodes (50.88 kJ mol^{-1}) (Fig. 3e), which indicates the improved Zn deposition kinetics for Pb@CF electrodes.

Moreover, preventing the stochastic diffusion of the deposited Zn atoms on the negative electrode is vital for curtailing Zn agglomeration and facilitating dendrite-free Zn deposition. The chronoamperometry test is conducted at constant working potentials to elucidate the diffusion processes of surface-adsorbed Zn^{2+} and Zn atoms on Pb@CF and CF electrodes (Fig. 3f)[42]. For a CF electrode, the current incrementally increases until achieving a steady state at 72 s, highlighting the augmentation of effective surface area due to prolonged and chaotic 2D diffusion of Zn, which fosters irregular Zn formation (Supplementary Fig. 12). In contrast, the chronoamperometry current of a Pb@CF electrode considerably exceeds that of the CF before reaching a steady state (25 s), which is likely coordinated with the formation of Pb seeds to activate additional nucleation sites. Then, the response current of the Pb@CF electrode is clearly reduced after stabilization compared to that of CF electrodes, which indicates that the swift nucleation on Pb@CF curtails the 2D diffusion of Zn^{2+} to achieve dense nucleation.

https://doi.org/10.1038/s41467-025-58473-3

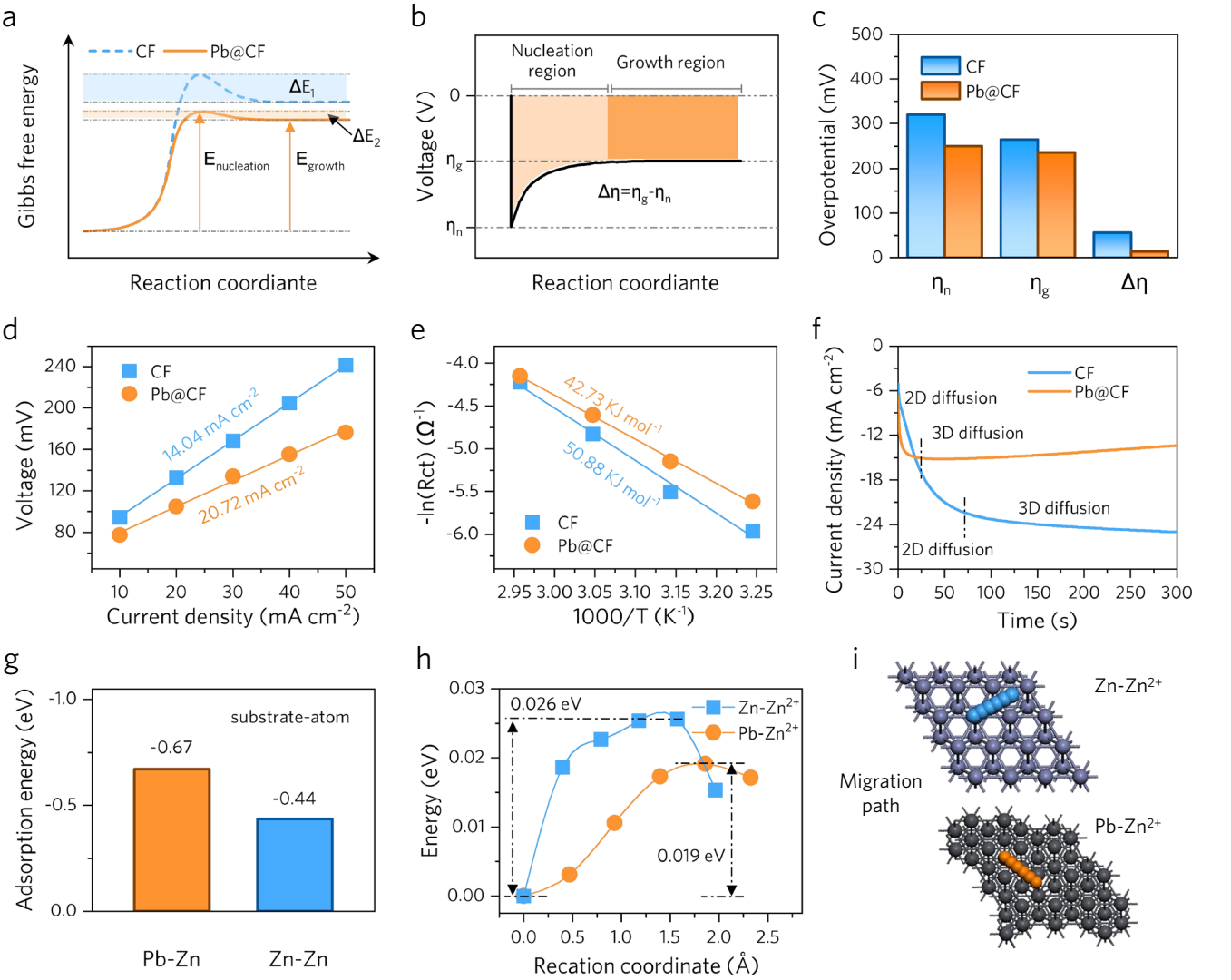

Fig. 3 | Zn deposition kinetics. a Illustration of the role of a Pb@CF electrode in tuning Zn nucleation and growth. **b** Typical voltage profiles of galvanostatic Zn deposition. **c** Corresponding overpotential values of Zn deposition at 40 mA cm^{-2} in different electrodes. **d** Exchange current density plots. **e** Desolvation energy from the Arrhenius equation. **f** Chronoamperogram profiles at an overpotential of -1.1 V. **g** Calculated absorption energies of Zn on different substrates. **h** Migration energy of Zn^{2+} on the Zn/Pb substrate, and (**i**) Corresponding migration path diagram (gray ball: Pb substrate, blue-gray ball: Zn substrate, blue/orange ball: Zn^{2+} on Zn/Pb substrate).

Density functional theory (DFT) computational analyses are conducted to explore the role of the deposited Pb nanoparticles in improving Zn deposition during the initial deposition stage. The adsorption energies of Zn atom on Pb, CF, and Zn substrates are -0.11 eV, -0.44 eV, and -0.67 eV, respectively (Fig. 3g and Supplementary Fig. 13). This suggests that the Pb substrate, *i.e.*, the Pb (111) surface, is more favorable for Zn atom deposition than the Zn (002) plane of CF. The choice of the Zn (002) plane is based on the XRD result of Zn deposited on the CF electrode (Supplementary Fig. 14), which is in agreement with previous studies[14]. Moreover, the Bader charge analysis indicates that more electrons are transferred to Zn atoms on the Pb substrate, demonstrating that Zn deposition on the Pb substrate is more energetically favorable than that on the Zn substrate (Supplementary Table 5). Furthermore, the migration energies of Zn^{2+} on different substrates are assessed to understand the subsequent Zn growth process (Fig. 3h, i, Supplementary Fig. 15). The migration energy of Zn^{2+} on the CF, Zn, and Pb substrates are 0.372 eV, 0.026 eV, and 0.019 eV, respectively, demonstrating that Zn^{2+} migrates faster on the Pb surface to inhibit the Zn aggregation on Pb substrate. In addition, in situ optical microscopy is used to inspect Zn deposition, and obvious dendrite configurations are observed on a CF electrode (Supplementary Fig. 16a). In contrast, a Pb@CF electrode demonstrates a compact Zn morphology devoid of significant protrusions (Supplementary Fig. 16b). These results further confirm the above calculation results that the Pb@CF electrode is more favorable for uniform Zn deposition.

Based on the above results, the nucleation and growth process of the Zn electrode on CF and Pb@CF electrodes are illustrated in Fig. 4. Zn nuclei on a CF electrode appear sporadically and rapidly due to limited nucleation sites, leading to the clustering of Zn atoms at specific sites and the subsequent formation of uneven dendrite deposits (Fig. 4a). In contrast, the Pb@CF electrode exhibits distinct behaviors that the abundant zincophilic Pb nanoparticles act as nucleation sites, which homogenizes and accelerates the nucleation process. It promotes the formation of a continuous, dense Zn layer, thus ensuring uniform Zn deposition across the electrode (Fig. 4b).

HER inhibition based on Pb@CF electrodes

The Pb@CF electrodes are characterized to evaluate their influence on the cycle stability of Zn negative electrodes, especially the CE

https://doi.org/10.1038/s41467-025-58473-3

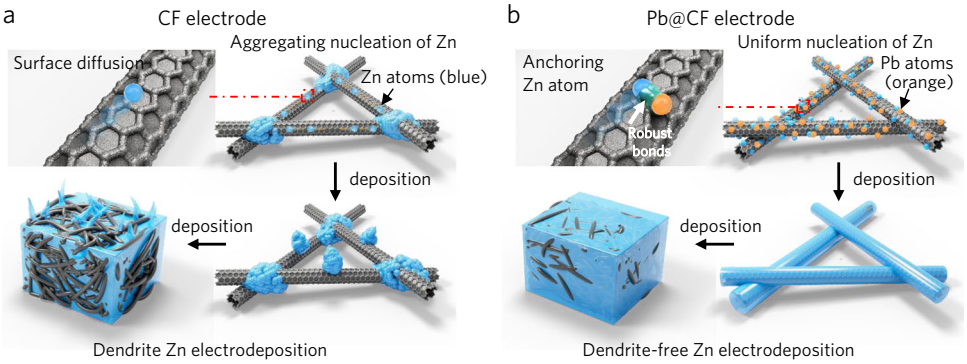

Fig. 4 | Illustration of different electrodes to regulate Zn nucleation and growth behaviors. a CF electrode and (**b**) Pb@CF electrode (gray ball: carbon substrate, blue ball: Zn atom, orange ball: Pb atom).

performance, in asymmetric Zn flow batteries (ASZFBs). Test methods are detailed in the Methods and the detailed components are presented in Supplementary Fig. 17. The initial CE (98.9%) with a Pb@CF exceed the 94.7% with the CF electrode (Supplementary Fig. 18). Furthermore, the Pb@CF-based ASZFBs demonstrate lower polarization overpotentials (322.3 mV compared to 417.3 mV for CF-based batteries), indicating the enhanced charge transfer kinetics and reduced internal resistance by utilizing the Pb@CF electrodes (Supplementary Fig. 19). During the cycling test, the Pb@CF-based ASZFBs consistently exhibit lower and stable voltage hysteresis (Supplementary Fig. 20) and achieve over 500 stable cycles with an average CE of 98.6% (Fig. 5a). Conversely, the CF-based ASZFBs show increasing voltage hysteresis and gradually decreased CE, which fail after 65 cycles (average CE: 96.5%). These results indicate the improved reversibility of the Zn negative electrode with Pb@CF, which can be attributed to the inhibition on the side reactions of HER, dendrite growth, and the dead Zn.

The electrochemical impedance spectroscopy results demonstrate the high internal resistance of CF-based ASZFBs, due to the existence of byproducts (Supplementary Fig. 21). Correspondingly, it is observed that the cycled electrolytes from the CF-based ASZFBs exhibit noticeable turbid, as shown in Fig. 5b. XRD analysis was conducted on the sediments in the cycled electrolyte based on CF electrodes, and the peaks were assigned to $Zn_5(OH)_8Cl_2{\cdot}H_2O$ (Fig. 5c). The turbid substance can result from side reactions, described in Eq. 3, which occur during Zn plating/stripping processes[43]:

$$3Zn(OH_2)_6^{2+} + 2Zn^{2+} + 2Cl^- + (2x-8)H^+ + 2xe^- \rightarrow Zn_5(OH)_8Cl_2H_2O + 9H_2O + xH_2\uparrow \quad (3)$$

These by-products are originated from the parasitic HER, resulting in the formation of irreversible $Zn_5(OH)_8Cl_2{\cdot}H_2O$. Post-operational analysis of the CF-based ZAFBs shows extensive dendrites morphology and dead Zn on its electrodes and membranes (Supplementary Figs. 22 and 23). Conversely, the Pb@CF-based ASZFBs maintain a clear electrolyte without forming byproducts, with the electrode and membrane exhibiting clean and smooth surfaces devoid of any Zn deposits (Supplementary Figs. 24 and 25). These observations indicate that Pb@CF effectively facilitates the uniform Zn deposition and simultaneously suppresses the undesirable HER side reactions.

The HER based on Pb@CF and CF electrodes are analyzed, where the initiation potentials are determined from the onset potential of hydrogen in a linear sweep voltammetry (LSV) curve. A delayed HER onset potential contributes to favoring stable Zn reduction and inhibiting HER[24]. LSV tests are conducted using 1 M Na_2SO_4 solution (eliminating the influence of Zn deposition current) to explore the effect of the Pb@CF electrodes in suppressing HER (Fig. 5d). Compared to CF electrodes, the Pb@CF electrodes maintain lower current density of hydrogen evolution reaction. Moreover, the onset potential for HER on Pb@CF electrodes shifts to -1.493 V from -1.419 V (vs. Ag/AgCl) for CF electrodes, indicating a suppressed HER.

Similarly, other composite electrodes incorporating heterometals, including Bi, In, and Sn, are fabricated via the electrodeposition method. The emergence of distinct reduction peaks in CV curves corresponding to the deposited metals on CF electrode (Supplementary Fig. 26). These composite electrodes (e.g. Bi@CF, In@CF, Sn@CF) also exhibit delayed hydrogen evolution onset potentials (-1.476 V, -1.459 V, -1.455 V) compared to the control CF electrodes (Supplementary Fig. 27), which indicates the universality of introducing heterometals to modify the electrode surface. Additionally, heterometal modification substantially improves the corrosion resistance of the electrodes in 2 M $ZnBr_2$ + 3 M KCl electrolytes. The Tafel plots show the advantageous impact of the Pb@CF electrodes on the corrosion resistance, as evidenced by an increment in corrosion potential from -0.96 V to -0.93 V relative to CF electrodes (Fig. 5e). This shift indicates the suppressed anti-corrosion capability of the deposited Zn metal on Pb@CF electrodes. Notably, the corrosion current of Pb@CF electrodes decreases by 1.51 mA cm^{-2} compared to CF electrodes. Corrosion currents of other composite electrodes (e.g. Bi@CF, In@CF, Sn@CF, et al.) are down by 1.17, 1.03, and 0.97 mA cm^{-2} (Supplementary Fig. 28) compared to CF, respectively. These findings indicate the beneficial role of heterometals in improving the thermodynamic stability of the electrode, thereby exemplifying the efficiency of this heterometal-based modification strategy. Among these composite electrodes, the Pb@CF electrode exhibits the lowest onset hydrogen evolution potential and demonstrates good corrosion resistance. Furthermore, the hydrogen evolution of different electrodes during Zn plating/stripping is quantitatively assessed using an in situ hydrogen evolution testing apparatus (see Methods). It shows the hydrogen evolution at Pb@CF electrodes is notably lower, registering 96 ppm compared to 427 ppm from the CF electrodes throughout the continuous plating-stripping testing for 23 h under 40 mA cm^{-2}/20 mAh cm^{-2} (Fig. 5f).

To further explore the underlying mechanism by which Pb@CF inhibits HER, the effect of Pb on HER is evaluated through the Gibbs free energy of H adsorption (ΔG_{H^*}), where the ΔG_{H^*} is a key parameter for evaluating the HER activity of various substrates[44,45]. A higher ΔG_{H^*} indicates a weaker affinity of H with substrate and thus effecctive HER suppression[25,26]. Accordingly, as shown in Supplementary Fig. 29, the calculated ΔG_{H^*} value for Pb substrates (1.17 eV) is obviously higher than the ΔG_{H^*} of Zn substrate (0.61 eV), demonstrating the improved capability of Pb@CF electrode in suppressing HER. Meanwhile, the ΔG_{H^*} of other substrates (e.g., the Bi, In, and Sn, respectively) are calculated, where the specfic crystal planes of these metal substrates are also determined based on the XRD results of composite electrodes (Supplementary Fig. 30). The corresponding ΔG_{H^*} values are 0.98 eV, 0.88 eV, and 0.69 eV, respectively, while their HER suppression

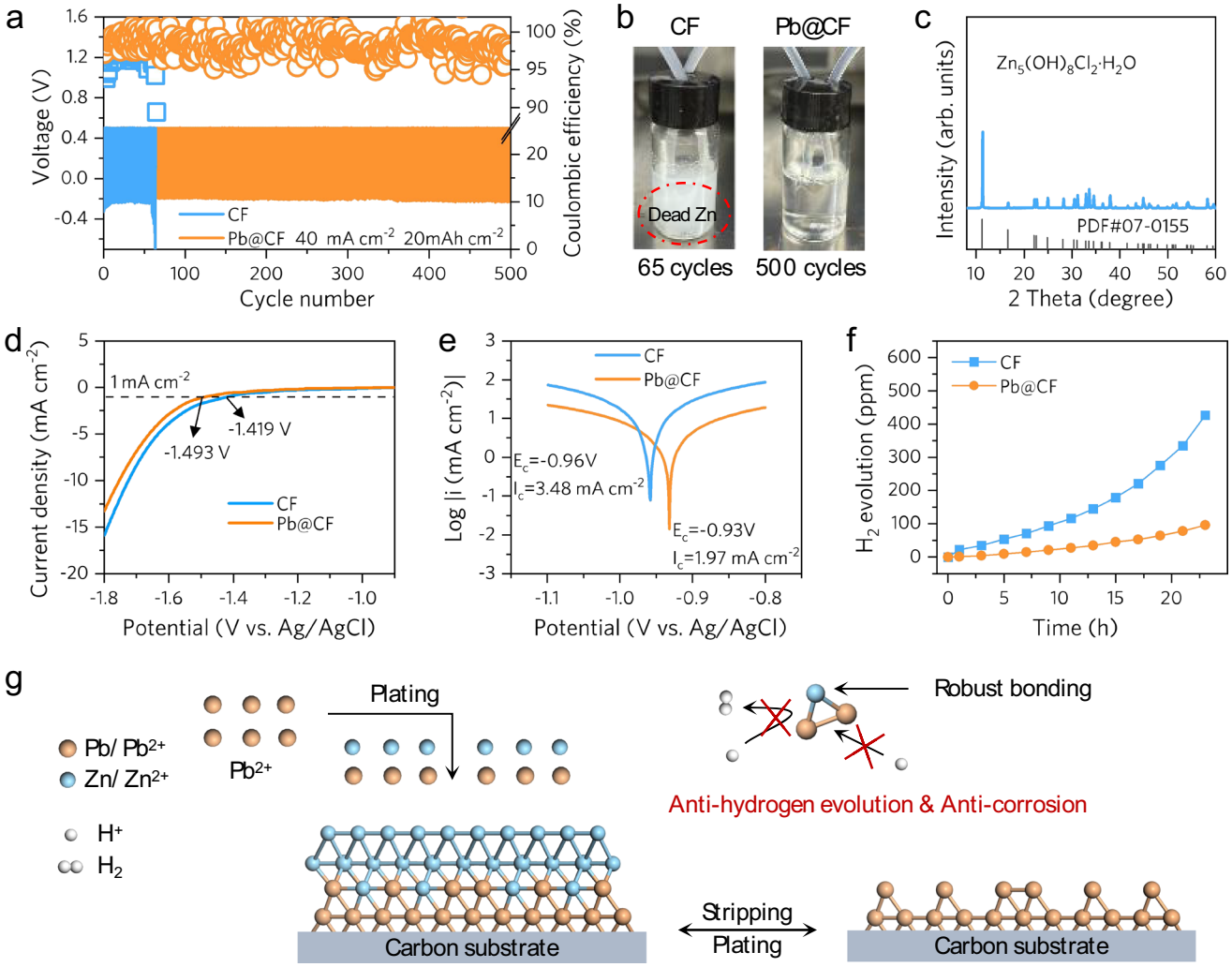

Fig. 5 | Anti-hydrogen evolution of a Pb@CF electrode on Zn deposition. a CE of an asymmetric Zn flow battery with 40 mA cm^{-2}/20 mAh cm^{-2}. **b** Optical photographs of electrolyte bottles after different cycles based on CF/Pb@CF electrodes. **c** XRD spectra of CF-based deposit. **d** LSV curves of the CF/Pb@CF electrode in 1 M Na_2SO_4 at 5 mV s^{-1}. **e** Tafel curves of the CF/Pb@CF electrode in 2 M $ZnBr_2$ + 3 M KCl electrolytes. **f** Hydrogen evolution testing. **g** Schematic describing the Pb@CF electrode in suppressing HER (white ball: H^+/H_2, blue ball: Zn atom, orange ball: Pb atom).

effectiveness is inferior compared to that of Pb (Supplementary Fig. 27 and 29). Additionally, the uniform zinc morphology based on the Pb@CF electrode further minimizes the tip effect, further mitigating competitive HER. As a result, the enhanced reversibility of Pb@CF electrodes can be attributed to the robust intermetallic bonding and the low affinity of Pb-Zn for H^+ to enable a dendrite-free morphology and suppress HER by anti-hydrogen evolution and anti-corrosion capability (Fig. 5g).

Stable cycling of Pb@CF electrode-based flow batteries

The rate performance of symmetric Zn flow batteries (SZFBs) is tested with Pb@CF and CF electrodes (Fig. 6a). The batteries with a Pb@CF electrode deliver consistently lower polarization potentials than those equipped with a CF electrode (Fig. 6b), when the current density varied as 10, 20, 30, 40, and 50 mA cm^{-2}. It is found that the Pb@CF electrode with the abundant zincophilic Pb sites significantly decreases the nucleation and growth overpotentials of Zn, thereby featuring a lower voltage hysteresis. The Pb@CF-based SZFBs achieve stable cycling over 5000 cycles (CPC: 20 Ah cm^{-2}) at 50 mA cm^{-2}/5 mAh cm^{-2} (Fig. 6c). Conversely, the CF-based SZFBs show significant voltage instability after 340 cycles, which can be ascribed to the irreversible Zn dendrites and HER. On the other side, the reversibility of the Pb@CF and CF electrodes is evaluated at a high current density and large areal capacity. Even under more demanding condition of 100 mA cm^{-2}/100 mAh cm^{-2} (Fig. 6d), the Pb@CF battery shows stable operation over 136 cycles (CPC: 13.6 Ah cm^{-2}), maintaining low polarization and steady voltage throughout the charge-discharge cycles (Fig. 6e). The CF-based battery exhibits severe voltage fluctuation after only five cycles, indicative of increased dendrite growth and side reactions that cause battery degradation. Notably, the voltage profile of the SZFB isn't a straight line, as illustrated in the magnified profile in Supplementary Fig. 31. Meanwhile, the EIS of the SZFB is performed before and after cycling, revealing no significant decrease in impedance after 10 cycles (Supplementary Fig. 32). Therefore, the SZFB is inconformity with the typical characteristics of a soft short circuit[46]. These results demonstrate improved stability of the Pb@CF electrode in Zn plating/stripping.

The electrochemical performance of the Pb@CF and the CF electrodes are comparatively tested in a full-cell configuration as ZBFBs (Fig. 7a). The Pb@CF-based ZBFBs maintain better efficiency and stability across varying current densities compared to CF electrodes (10–40 mA cm^{-2}), showcasing its capability for stable energy storage across a wide power spectrum (Fig. 7b and Supplementary Figs. 33–36). The Pb@CF-based ZBFBs deliver lower discharge polarization and higher power density, with a peak of 192.3 mW cm^{-2} compared to 156.7 mW cm^{-2} for CF electrodes, evidencing significant

https://doi.org/10.1038/s41467-025-58473-3

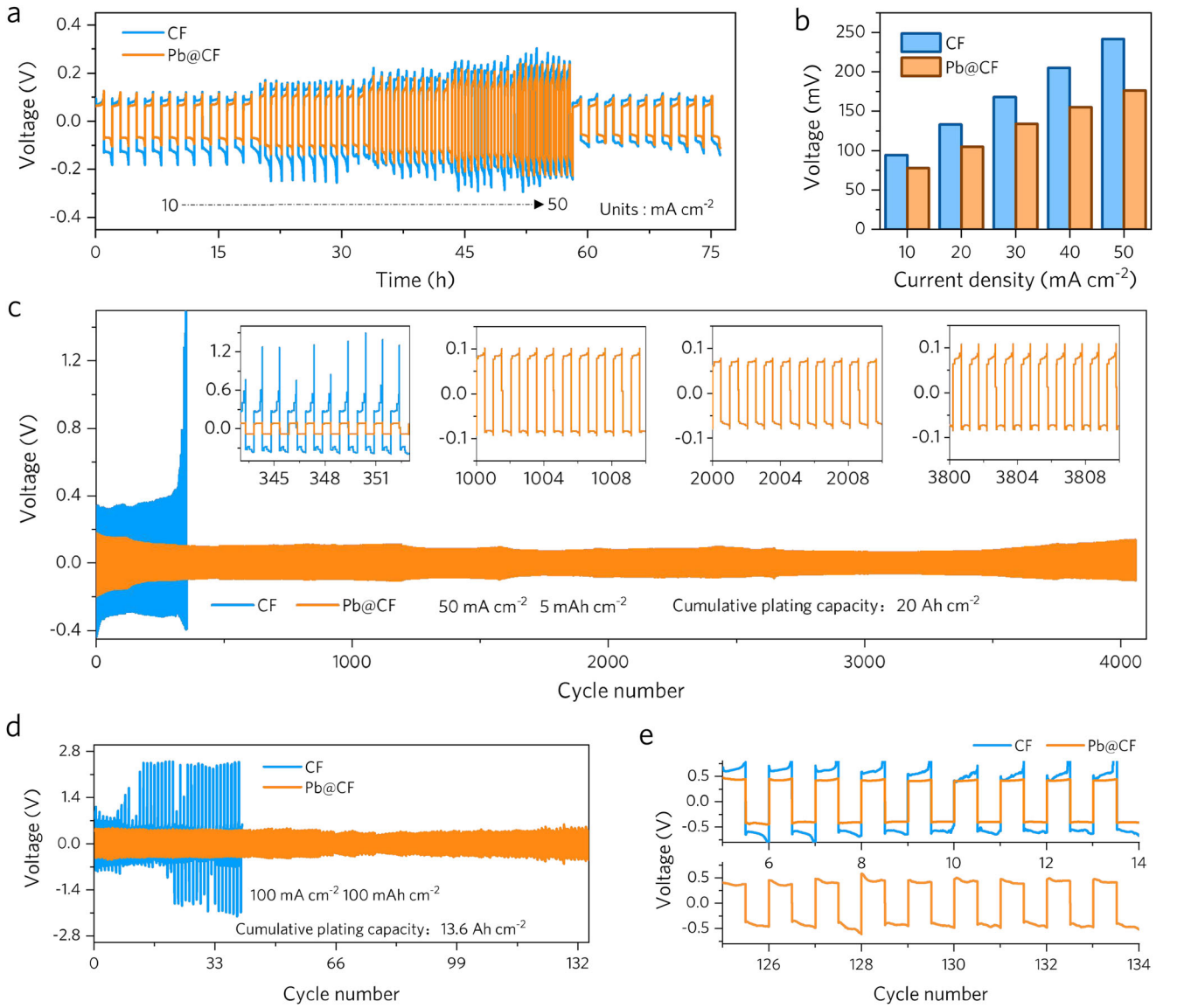

Fig. 6 | Reversibility test for Zn plating/stripping with different electrodes. **a** Rate performances of SZFBs at different current densities with a fixed capacity of 20 mAh cm^{-2}, and (**b**) summarized corresponding polarization potential values at different working currents. Cycle stability of SZFBs under different conditions: **c** 50 mA cm^{-2}/5 mAh cm^{-2} and the insets show local voltage profiles of different cycles. **d** Cycling performance conducted at 100 mA cm^{-2}/100 mAh cm^{-2}, and (**e**) corresponding voltage profiles after different cycles with 100 mA cm^{-2}/100 mAh cm^{-2}.

improvements in Zn^{2+}/Zn reaction kinetics and reversibility (Fig. 7c). In long-term cycle stability evaluations, Pb@CF-based ZBFBs maintain stable charging-discharging profiles over 2300 cycles at 20 mA cm^{-2}, achieving average CE (97.4%) and energy efficiency (EE) (78.0%), as well as a cumulative plating capacity of 23 Ah cm^{-2} (Fig. 7d, e and Supplementary Fig. 37). In contrast, the CF-based ZBFBs experience a performance degradation after 160 cycles (Supplementary Fig. 38), with charge-discharge curves becoming fluctuated by the 170th cycle. This instability is due to the dendrite growth and HER-induced inactive byproducts and accumulated dead Zn, resulting in poor average CE/EE (96.5%/77.8%). During high-power test condition under 40 mA cm^{-2}, the Pb@CF-based ZBFBs demonstrate higher efficiency over 1500 cycles (average CE and EE of 98.7% and 73.1%, respectively) (Fig. 7f and Supplementary Fig. 39) compared to the CF-based ZBFBs, which degrade rapidly after 175 cycles (Supplementary Fig. 40). Even under more stringent operation conditions (80 mA cm^{-2}/20 mAh cm^{-2}), the Pb@CF-based ZBFB exhibits stable cycling performance over 570 cycles, with an average CE and EE of 99.4% and 65.9%, respectively (Supplementary Fig. 41). In contrast, the CF-based ZBFB experiences rapid performance decay, failing after only 65 cycles (Supplementary Fig. 42). Notably, the charging voltage of the CF-based battery increased significantly at the 10th cycle (Supplementary Fig. 43), indicating deteriorating electrode reversibility. This degradation is further corroborated by EIS measurements, which reveals a pronounced increase in the impedance of the CF-based battery at the 10th cycle. Conversely, the Pb@CF-based battery features minimal impedance change, underscoring its enhanced reversibility and stability under severe operating conditions. Meanwhile, static zinc-bromine soft pack batteries assembled with the Pb@Zn negative electrode, where the nano-Pb particles are introduced onto the Zn foil electrode based our previous in situ substitution strategy[47], and it can deliver a stable 200 cycles and embody the efficiency of the Pb@Zn negative electrode for static zinc-bromine battery (Supplementary Fig. 44). The comparative analysis shows that the cycling stability and the CPC of the Pb@CF-based ZBFBs have surpassed previously documented performance levels for ZBFBs (Fig. 7g and Supplementary Table 1). This methodology provides a highly reversible electrode design guidance for achieving

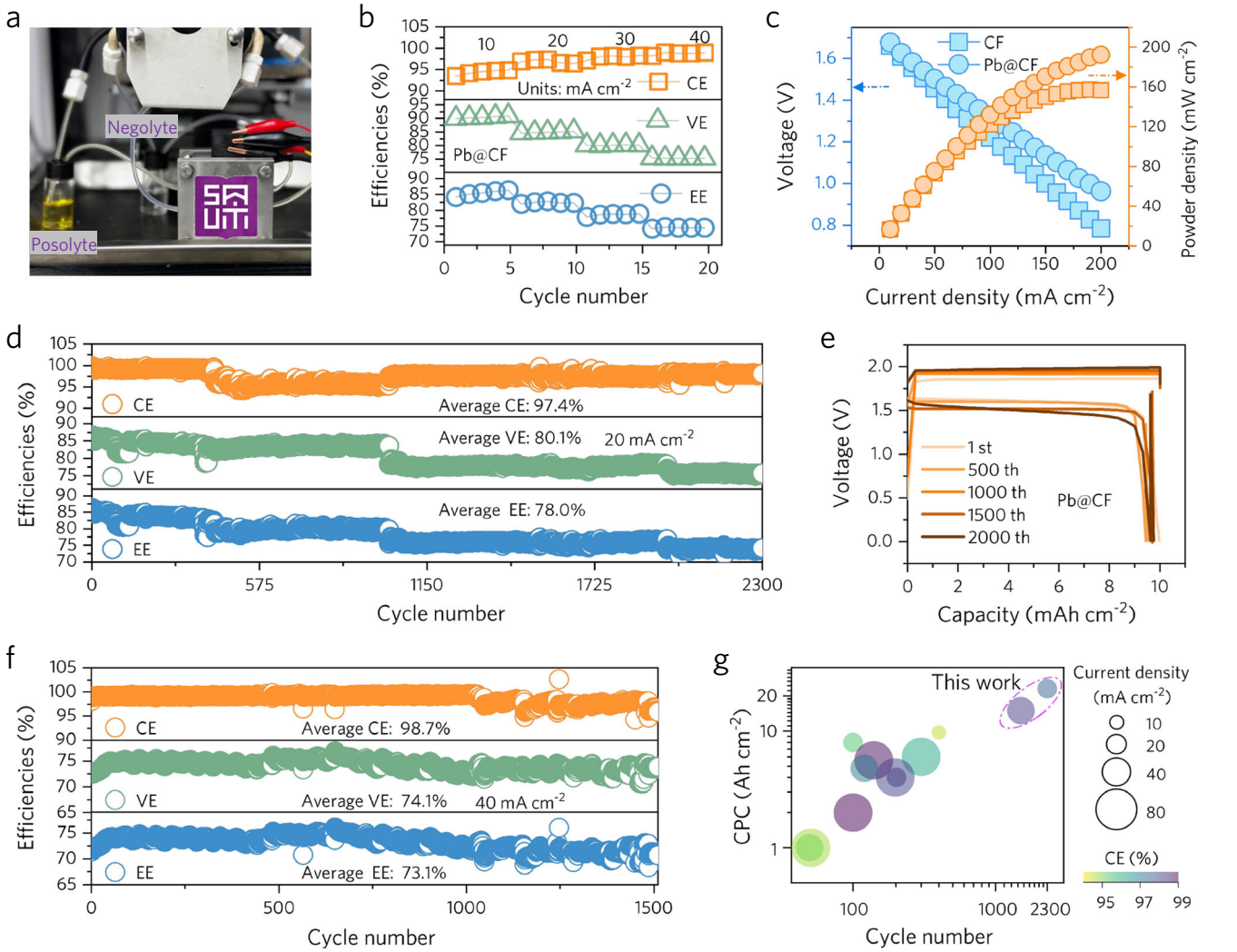

Fig. 7 | Electrochemical performance of ZBFBs. a Prototypical configuration of a ZBFB with a 4 cm^2 active working area (10 ml of posolyte and negolyte, respectively). **b** Coulombic efficiency (CE), voltage efficiency (VE) and energy efficiency (EE) of the ZBFBs with a Pb@CF electrode. **c** Discharge polarization and power density curves of the ZBFBs with a CF/Pb@CF electrode. **d** Long-term cycling efficiency of the ZBFBs at 20 mA cm^{-2} with a Pb@CF electrode during 2300 cycles/2300 h, and (**e**) the corresponding capacity-voltage profiles at different cycles. **f** Long-term cycling efficiency tests of the ZBFBs at 40 mA cm^{-2} with a Pb@CF electrode during 1500 cycles. **g** Comparison of operating current density, CE, cycle number, and CPC among various ZBFBs, where the detailed information are listed in Supplementary Table 1.

dendrite-free Zn deposition and demonstrates a broad potential in neutral or near-neutral systems.

Discussion

In summary, we develop a highly reversible Pb@CF electrode via a facile and effective in situ electrodeposition strategy to enable high reversibility and stability of Zn negative electrodes for ZBFBs. The abundant and uniformly distributed Pb nanoparticles act as zincophilic nucleation sites to interact with Zn atoms, which effectively promotes even Zn nucleation and prevents dendrite growth. This ensures smooth and dendrite-free Zn deposition, and meanwhile, the high HER overpotential of the Pb@CF electrode effectively inhibits the competing hydrogen evolution. Consequently, Pb@CF-based SZFBs realize a stable cycle life of over 4000 cycles at 50 mA cm^{-2} and achieve the CPC of 20 Ah cm^{-2}, showcasing their robust performance in challenging conditions. Even under an ultra-high current density/areal capacity (100 mA cm^{-2}/100 mAh cm^{-2}), the Pb@CF electrode can effectively inhibit dendrite growth and hydrogen evolution (CPC: 13.6 Ah cm^{-2}). Meanwhile, Pb@CF-based ZBFBs exhibit improved electrochemical performance with a cycling stability of over 2300 cycles (2300 h), an average CE above 97.4%, and a high CPC of 23 Ah cm^{-2}. Our work offers a straightforward yet feasible solution to suppress dendrite growth and inhibit the competing HER, and proposes an anodic electrode design strategy for improving the reversibility of Zn negative electrodes.

Methods

Materials

All chemicals were used without further purification. Zinc bromide ($ZnBr_2$, ≥98%), potassium chloride (KCl, ≥99%), 1-ethyl−1-methylpyrrolidinium bromide (MEP, ≥99%), sodium sulfate (Na_2SO_4, ≥99%), lead sulfate ($PbSO_4$, ≥98%), bismuth chloride ($BiCl_3$, Reagent Grade), indium trichloride ($InCl_3{\cdot}4H_2O$, ≥98%), stannous chloride ($SnCl_2{\cdot}2H_2O$, ≥98%), Tetrabutylammonium Tribromide ($TBABr_3$, ≥98%, molecular weight: 482.17), and 1-Methyl-2-pyrrolidinone (NMP, ≥99%) were obtained from Aladdin. Activated carbon (TIMCAL), ketjen black (KB, ECP-600JD), and poly(vinylidene fluoride) (HSV900) were obtained from Guangdong Canrd New Energy Technology Co.,Ltd. Zinc foil (0.1 mm and 0.2 mm, 99.99%) and Titanium foil (0.1 mm, 99.99%) were purchased from Shengshida Metal Material Co., Ltd. Glass microfiber

binder free filter serving as separator purchases from Whatman (1825-047, 0.7 Micron, 19 s/100 mL Flow Rate, Grade GF/F, 4.7 cm Diameter). Carbon felt (3.0 mm, carbon content ≥99%, bulk density 0.12-0.14 g cm^{-3}) was obtained from Yi Deshang Carbon Technology. Carbon paper (HCP010N) was acquired from Shengernuo Energy Store. A porous polyolefin membrane (20 nm average pore size, 55 ~ 60% porosity, 600 μm thickness) was purchased from Wuhan Zhisheng. A hydrogen tester (BX-168) was acquired from the Aidekesi Flagship Store.

Preparation of electrolytes

Electrolytes used for electrochemical and symmetrical/asymmetrical Zn flow batteries (SZFBs/ASZFBs) testing were prepared as follows at an average of 25 °C ± 0.5 °C and without gas protection. The baseline electrolyte consisted of 2 M $ZnBr_2$ and 3 M KCl. The modified electrolyte was composed of 2 M $ZnBr_2$, 3 M KCl, and 1 mM $PbSO_4$. The electrolytes in ZBFBs were prepared as follows. The baseline electrolytes, including both posolyte and negolyte, consisted of 2 M $ZnBr_2$, 3 M KCl, and 0.4 M MEP. The modified negolyte was prepared with 2 M $ZnBr_2$, 3 M KCl, 0.4 M MEP, and 1 mM $PbSO_4$. The posolyte was composed of 2 M $ZnBr_2$, 3 M KCl, and 0.4 M MEP. Unless otherwise specified, the baseline electrolyte was used with CF electrodes, while the modified electrolyte was applied to Pb@CF electrodes. The electrolyte for the preparation of other composite electrodes consisted of 2 M $ZnBr_2$, 3 M KCl, and 1 mM $BiCl_3$/$InCl_3{\cdot}4H_2O$/$SnCl_2{\cdot}2H_2O$. 20uL HCl was added to $BiCl_3$ to help it dissolve.

Preparation the Pb@CF electrode

Carbon felt electrodes were washed sequentially with deionized water and anhydrous ethanol by ultrasonic cleaning, and then dried in an oven at an average 60°C ± 0.5°C for complete removal of moisture. For Pb@CF electrodes used in non-battery testing (carbon felts were cut into 1 cm * 2 cm with a reaction area of 1 cm^2), Pb nanoparticles were deposited onto the CF substrate using an electrochemical deposition method. A three-electrode system was employed, with the CF electrode as the working electrode, an Ag/AgCl electrode as the reference electrode, and a platinum sheet as the counter electrode. Electrochemical deposition was performed in a 1 mM $PbSO_4$ solution. Deposition occurred at potentials of −0.65 V versus an Ag/AgCl reference electrode. The deposition process was conducted under an average 25 °C ± 0.5 °C without any gas protection. The applied potential range and current density during deposition were optimized to ensure uniform Pb nanoparticle formation on the CF surface. For Pb@CF electrodes used in battery testing (carbon felts were cut into 2 cm × 2 cm with a reaction area of 4 cm^2), Pb nanoparticles were deposited in situ during the first cycle of battery operation. This process occurred under the same temperature, without gas protection.

Symmetrical/asymmetrical Zn flow batteries (SZFBs/ASZFBs) and Zn bromine flow batteries (ZBFBs) assembly

SZFBs, ASZFBs, and ZBFBs were constructed using zinc foil (2 × 2 cm) and carbon felt (2 × 2 cm) as electrodes, separated by a porous polyolefin membrane, with 10 mL of circulating electrolyte per electrode. Specifically, SZFBs employed a combination of zinc foil and carbon felt as both negative and positive electrodes. In ASZFBs and ZBFBs, zinc foil and carbon felt composite as the negative electrode, carbon felt as the positive electrode. In ASZFBs, the Zn foil + carbon felt electrode acted as a Zn reservoir to facilitate the analysis of reaction reversibility at the working electrode. Additionally, the electrolyte circulation rates were maintained at 50 mL min^{-1} for both the negolyte and posolyte reservoirs during all flow battery tests.

Electrochemical measurement

All these electrochemical tests were carried out at an average 25 °C ± 0.5 °C, no climatic/environmental chamber was used, and the iR-correction was not performed. The chronoamperometry, linear scanning voltammetry, and Tafel tests were conducted in baseline/modified electrolytes on a CHI 760E instrument. The chronoamperometry test was performed at fixed voltages in a three-electrode system (glassy carbon electrode (2.5 mm diameter, BAS Inc, Japan) or carbon felt, Ag/AgCl electrode, and Zn foil as working, counter, and reference electrode, respectively). The corresponding hydrogen evolution activity and corrosion resistance of different electrodes were investigated in a three-electrode system (Ag/AgCl electrode, Zn foil, and CF/Pb@CF as reference, counter, and working electrode, respectively) via a linear scanning voltammetry and Tafel with a scanning speed of 5 mV s^{-1}. The electrochemical impedance spectroscopy (EIS) measurements were carried out on a CHI electrochemical testing unit (760E). The EIS measurements were conducted under potentiostatic conditions. An AC signal amplitude of 5 mV was used. The measurements were performed over a frequency range of 100 kHz to 0.01 Hz. Before the EIS measurements, the system was stabilized at the open-circuit voltage for 10 min to achieve a quasi-stationary state. The in situ observation of Zn electroplating was conducted using an optical microscope. The constant current characteristics of SZFBs, ASZFBs, and ZBFBs were evaluated using a battery test system (LAND, CT2001A) at room temperature. The SZFBs test involved plating Zn at 5 mAh cm^{-2} and 100 mAh cm^{-2} onto the collectors at currents of 50 mA cm^{-2} and 100 mA cm^{-2}, respectively, followed by stripping Zn at the same current densities. The ASZFBs test involved plating Zn at 20 mAh cm^{-2} onto the substrates at 40 mA cm^{-2}, followed by stripping Zn at the same current until a cut-off voltage of 0.5 V was reached. The charging process of ZBFBs was constrained by a fixed capacity (10 mAh cm^{-2} or 20 mAh cm^{-2}), with a discharge cut-off voltage set at 0.01 V. During the discharge process, the initial discharge was performed at the charge current, followed by removing the remaining charge at a quarter of the initial discharge current.

In situ hydrogen evolution test

For the in situ hydrogen evolution test, a test setup based on a modified asymmetric zinc flow battery was used to detect the concentration of produced hydrogen. The carbon felt was cut and sonicated in ethanol and deionized water for 10 min each. The Pb@CF electrode was prepared in situ during the test. For the in situ hydrogen evolution test, we used a test setup based on a modified asymmetric zinc flow battery to detect the concentration of hydrogen produced, where the asymmetric cell having the CF as working electrode and the CF/Zn foil as counter electrode, respectively, based on a porous polyolefin membrane. The baseline electrolyte consists of 2 M $ZnBr_2$ and 3 M KCl for both working and counter electrodes, and the sole difference in posolyte is the addition of 1 mM $PbSO_4$ for the Pb@CF electrode. The volume of posolyte and negolyte is both 10 mL to circulate through the electrodes. The electrolyte bottle for the working electrode side is hermetically connected to the hydrogen tester. Hydrogen evolution was monitored during plating/stripping at a current density of 40 mA cm^{-2}. The produced hydrogen was detected at different times during battery operation using a hydrogen detector connected to the positive electrolyte bottle.

Preparation, assembly, and testing of static zinc-bromine batteries

The preparation of the $TPABr_3$ electrode involves the use of $TPABr_3$, activated carbon, Ketjen Black, and poly(vinylidene fluoride) as the active material, conductive additives, and binder. These materials were mixed in N-methylpyrrolidone solvent at a mass ratio of 3.5:3.5:2:1. The concentration of poly(vinylidene fluoride) in N-methylpyrrolidone is 10 mg/mL. Electrodes (titanium and zinc foils) cut into 1*2 cm^2 using a laser cutter (Super scan, SS-10-DA, $\lambda = 355$ nm). The slurry was then cast onto titanium foil using a Doctor blade method. The prepared electrode was dried at an average 60 °C ± 0.5 °C in a controlled humidity

environment for 12 h. The average mass loading of $TPABr_3$ in the electrode was 10.0 mg cm^{-2}. The zinc foil (0.1 mm thickness) was used as the negative current collector. No additional treatments were applied to the current collectors prior to electrode fabrication. Glass fiber separators were placed between the electrodes, and the electrolyte consisted of 0.5 M $ZnBr_2$, 0.2 M 1-ethyl-1-methylpyrrolidinium bromide, and 1 mM $PbSO_4$. A volume of 100 µL of electrolyte was used per cell. The cells were galvanostatically charged and discharged on a Land BT2001A battery test system at an average 25 °C ± 0.5 °C. The charge and discharge cut-off voltages were set at 1.9 V and 0.5 V, respectively.

Calculation of cumulative plating capacity

The cumulative plating capacity is calculated by multiplying area capacity per cycle by the total cycle numbers of Zn plating. This calculation is based on the cycling results of symmetric Zn flow batteries or Zn-bromine flow batteries, either from the literature or our study.

Material characterization

The morphologies of Zn deposits on carbon felt were analyzed via scanning electron microscopy (SEM) using a JSM-6300 (JEOL, Japan). Additionally, atomic force microscopy (AFM, Asylum Research) was utilized to observe Zn growth under different electrolytes, and Zn foil served as the substrate. The crystalline structures of the deposited Zn were characterized using X-ray diffraction (XRD) with a Bruker D8 Advance Kα-ray diffractometer ($\lambda = 1.54056$ Å). At the ex situ XRD measurements of Pb@CF electrodes, electrodes deposited for the appropriate duration were carefully removed for the XRD measurements using tweezers that had been pre-washed and dried to avoid contact with impurities at an average 25 °C ± 0.5 °C. After each XRD measurement, the electrodes were carefully placed back in using the tweezers for further deposition. This is repeated several times until the test is completed. At the XRD characterization of turbid matter in CF-based electrode cycling electrolyte solutions, the electrolyte solution bottles were first allowed to settle thoroughly. Any excess upper layer of the electrolyte solution was carefully aspirated using a pipette. Subsequently, deionized water was introduced into the bottle, and the turbid matter was subjected to ultrasonic cleaning treatment for 10 min. After ultrasonication, the turbid matter was allowed to settle again, and the clear supernatant was carefully aspirated. The residue was washed sequentially with deionized water and anhydrous ethanol, each step repeated three times. Finally, the sample was dried in a vacuum oven at 60 °C ± 0.5 °C for 12 h to ensure complete dehydration prior to XRD analysis. Quantitative gas production tests were conducted using a hydrogen testing apparatus.

Density functional theory (DFT) calculation

First-principles density functional theory (DFT) calculations were carried out using the Vienna ab initio simulation package (VASP)[48] and the DS-PAW software package[49] with the plane-wave basis projector augmented wave (PAW) method. The exchange-correlation energy function was described using a revised Perdew-Burke-Ernzerhof (PBE) version of the generalized gradient approximation (GGA)[50]. For the slab calculations, the Gaussian smearing method was employed with a smearing width of 0.05 eV. To eliminate the interaction between the top and bottom surfaces due to periodicity, a vacuum spacing of 15 Å was set along the z-direction. Lead (111) and zinc (002) surfaces were used to calculate surfaces. It is important to note that van der Waals (vdW) corrections were not included in our calculations. While incorporating vdW corrections could lead to slight quantitative refinements in the calculated adsorption energies[51], it would not alter the relative trends or the qualitative conclusions of our study (Supplementary Fig. 45). The calculation parameters and configurations of lead and zinc in Supplementary Data 1-4.

The adsorption energy (E_{ads}) was calculated as:

$$E_{\mathrm{ads}} = E_{\mathrm{system}} - (E_{\mathrm{slab}} + E_{\mathrm{adsorbate}}) \tag{4}$$

where E_{system} is the total energy of the catalysts system with adsorbates, E_{slab} is the total energy of the bare slab, and $E_{\mathrm{adsorbate}}$ is the total energy of the isolated adsorbate in vacuum. According to this definition, a more negative value of adsorption energy indicates a thermodynamically favorable configuration, signifying that the adsorption process was exothermic.

To obtain the transition states and Zn-ion migration barriers, we used the climbing image nudged elastic band (CI-NEB) method[52,53]. The force convergence criteria were set to 0.03 eV/Å. The calculation parameters for NEB and the corresponding initial and final configurations of Zn atoms on Pb and Zn in Supplementary Data 5-6.

The hydrogen adsorption energies (ΔG_{H^*}) is defned as:

$$\Delta E_{\mathrm{H}^*} = \frac{E_{\mathrm{nH}^*} - E_{\mathrm{slab}} - \frac{\mathrm{n}}{2} E_{\mathrm{H_2}}}{\mathrm{n}} \tag{5}$$

where E_{nH^*} is the total energy of the slab with n H atoms adsorbed, E_{Zn} is the energy of the specify slab model, and E_{H_2} is the energy of the H_2 molecule in the gas phase state.

The hydrogen adsorption free energies (ΔG_{H^*}) were calculated as[45]:

$$\Delta G_{\mathrm{H}^*} = \Delta E_{\mathrm{H}^*} + \Delta ZPE - T\Delta S$$

$$= \Delta E_{\mathrm{H}^*} + ZPE_{H^*} - \frac{1}{2} ZPE_{\mathrm{H_2}} - TS_{\mathrm{H}^*} + \frac{1}{2} TS_{\mathrm{H_2}} \tag{6}$$

where the ΔE_{H^*} is defined in Eq. (5). The temperature is set to 298.15 K. The ZPE_{H^*}, S_{H^*}, ZPE_{H_2}, and S_{H_2} are the zero-point vibration energy and entropy of H that adsorbed on Zn surface and gas phase H_2 under standard atmospheric pressure, respectively.

Data availability

All data that support the findings of this study are presented in the manuscript and Supplementary Information. Source data are provided with this paper.

References

1. Zuo, P. et al. Near-frictionless ion transport within triazine framework membranes. *Nature* **617**, 299–305 (2023).
2. Obama, B. The irreversible momentum of clean energy. *Science* **355**, 126–129 (2017).
3. Soloveichik, G. L. Flow Batteries: current status and trends. *Chem. Rev.* **115**, 11533–11558 (2015).
4. Park, M. et al. Material design and engineering of next-generation flow-battery technologies. *Nat. Rev. Mater.* **2**, 16080 (2017).
5. Yao, Y., Lei, J., Shi, Y., Ai, F. & Lu, Y. C. Assessment methods and performance metrics for redox flow batteries. *Nat. Energy* **6**, 582–588 (2021).
6. Wei, Z. et al. Starch-mediated colloidal chemistry for highly reversible zinc-based polyiodide redox flow batteries. *Nat. Commun.* **15**, 3841 (2024).
7. Ling, R. et al. Dual-function electrolyte additive design for long life alkaline zinc flow batteries. *Adv. Mater.* **36**, 2404834 (2024).
8. Tang, L., Li, T., Lu, W. & Li, X. Reversible solid bromine complexation into $Ti_3C_2T_x$ MXene carriers: a highly active electrode for bromine-based flow batteries with ultralow self-discharge. *Energy Environ. Sci.* **17**, 3136–3145 (2024).
9. Yang, J. et al. Synergetic modulation on solvation structure and electrode interface enables a highly reversible zinc anode for zinc-iron flow batteries. *ACS Energy Lett.* **7**, 2331–2339 (2022).

10. Wu, M. C., Zhao, T. S., Wei, L., Jiang, H. R. & Zhang, R. H. Improved electrolyte for zinc-bromine flow batteries. *J. Power Sources* **384**, 232–239 (2018).
11. Liu, B. et al. Developing terpyridine-based metal complexes for non-aqueous redox flow batteries. *Energy Storage Mater.* **60**, 102808 (2023).
12. Zhang, Q. et al. Redox-targeting catalyst developing new reaction path for high-power zinc-bromine flow batteries. *J. Power Sources* **601**, 234286 (2024).
13. Huang, S. et al. A redox-mediated zinc electrode for ultra-robust deep-cycle redox flow batteries. *Energy Environ. Sci.* **16**, 438–445 (2022).
14. Wang, S. et al. A highly reversible zinc deposition for flow batteries regulated by critical concentration induced nucleation. *Energy Environ. Sci.* **14**, 4077–4084 (2021).
15. Lai, Q., Zhang, H., Li, X., Zhang, L. & Cheng, Y. A novel single flow zinc-bromine battery with improved energy density. *J. Power Sources* **235**, 1–4 (2013).
16. Jiang, H. R., Wu, M. C., Ren, Y. X., Shyy, W. & Zhao, T. S. Towards a uniform distribution of zinc in the negative electrode for zinc bromine flow batteries. *Appl. Energy* **213**, 366–374 (2018).
17. Ortiz-Aparicio, J. L. et al. Effects of organic additives on zinc electrodeposition from alkaline electrolytes. *J. Appl. Electrochem.* **43**, 289–300 (2013).
18. Banik, S. J. & Akolkar, R. Suppressing dendrite growth during zinc electrodeposition by PEG-200 additive. *J. Electrochem. Soc.* **160**, 519–523 (2013).
19. Bani Hashemi, A., Kasiri, G. & La Mantia, F. The effect of polyethyleneimine as an electrolyte additive on zinc electrodeposition mechanism in aqueous zinc-ion batteries. *Electrochim. Acta* **258**, 703–708 (2017).
20. Hu, J., Yue, M., Zhang, H., Yuan, Z. & Li, X. A boron nitride nanosheets composite membrane for a long-life zinc-based flow battery. *Angew. Chem. Int. Ed.* **59**, 6715–6719 (2020).
21. Yuan, Z. et al. Negatively charged nanoporous membrane for a dendrite-free alkaline zinc-based flow battery with long cycle life. *Nat. Commun.* **9**, 3731 (2018).
22. Yin, Y. et al. Dendrite-free zinc deposition induced by tin-modified multifunctional 3D host for stable zinc-based flow battery. *Adv. Mater.* **32**, 1906803 (2020).
23. Ma, L. et al. Realizing high zinc reversibility in rechargeable batteries. *Nat. Energy* **5**, 743–749 (2020).
24. Xiao, P. et al. An anticorrosive zinc metal anode with ultra-long cycle life over one year. *Energy Environ. Sci.* **15**, 1638–1646 (2022).
25. Wang, L. et al. Screening selection of hydrogen evolution-inhibiting and zincphilic alloy anode for aqueous Zn battery. *Adv. Sci.* **11**, 1–9 (2024).
26. Li, R. et al. Alloying strategy for high-performance zinc metal anodes. *ACS Energy Lett.* **8**, 457–476 (2023).
27. Ruan, P. et al. Achieving highly proton-resistant Zn–Pb anode through low hydrogen affinity and strong bonding for long-life electrolytic Zn//MnO_2 battery. *Adv. Mater.* **35**, 2300577 (2023).
28. Fan, X. et al. Enabling stable Zn anode via a facile alloying strategy and 3D foam structure. *Adv. Mater. Interfaces* **8**, 1–9 (2021).
29. Zhao, Y. et al. Tailoring grain boundary stability of zinc-titanium alloy for long-lasting aqueous zinc batteries. *Nat. Commun.* **14**, 7080 (2023).
30. Su, J. et al. Temperature-dependent nucleation and electrochemical performance of Zn metal anodes. *Nano Lett.* **22**, 1549–1556 (2022).
31. Chen, S. et al. Enabling low-temperature and high-rate Zn metal batteries by activating Zn nucleation with sngle-atomic sites. *ACS Energy Lett.* **7**, 4028–4035 (2022).
32. Sanz, E. et al. Homogeneous ice nucleation at moderate supercooling from molecular simulation. *J. Am. Chem. Soc.* **135**, 15008–15017 (2013).
33. Jana, A. & García, R. E. Lithium dendrite growth mechanisms in liquid electrolytes. *Nano Energy* **41**, 552–565 (2017).
34. Li, C. et al. Highly reversible Zn anode with a practical areal capacity enabled by a sustainable electrolyte and superacid interfacial chemistry. *Joule* **6**, 1103–1120 (2022).
35. Zhu, Y. et al. Engineering hosts for Zn anodes in aqueous Zn-ion batteries. *Energy Environ. Sci.* **17**, 369–385 (2023).
36. Zhang, Q., Luan, J., Tang, Y., Ji, X. & Wang, H. Interfacial design of dendrite-free zinc anodes for aqueous zinc-ion batteries. *Angew. Chem. Int. Ed.* **59**, 13180–13191 (2020).
37. Ely, D. R. & García, R. E. Heterogeneous nucleation and growth of lithium electrodeposits on negative electrodes. *J. Electrochem. Soc.* **160**, A662–A668 (2013).
38. Pei, A., Zheng, G., Shi, F., Li, Y. & Cui, Y. Nanoscale nucleation and growth of electrodeposited lithium metal. *Nano Lett.* **17**, 1132–1139 (2017).
39. Jiao, S. et al. Ion sieve: tailoring Zn^{2+} desolvation kinetics and flux toward dendrite-free metallic zinc anodes. *ACS Nano* **16**, 1013–1024 (2022).
40. Hu, Y., Fu, J., Hu, H., Ho, D. & Hu, H. Differentiating contribution to desolvation ability from molecular structure and composition for screening highly-effective additives to boost reversibility of zinc metal anode. *Energy Storage Mater.* **55**, 669–679 (2023).
41. Yang, Y. et al. Weakly solvating effect spawning reliable interfacial chemistry for aqueous Zn/Na hybrid batteries. *Adv. Energy Mater.* **13**, 2203729 (2023).
42. Dai, Y. et al. Reversible Zn metal anodes enabled by trace amounts of underpotential deposition initiators. *Angew. Chem. Int. Ed.* **62**, e202301192 (2023).
43. Qian, L. et al. Cations coordination-regulated reversibility enhancement for aqueous Zn-ion battery. *Adv. Funct. Mater.* **31**, 2105736 (2021).
44. Greeley, J., Jaramillo, T. F., Bonde, J., Chorkendorff, I. & Nørskov, J. K. Computational high-throughput screening of electrocatalytic materials for hydrogen evolution. *Nat. Mater.* **5**, 909–913 (2006).
45. Zhao, R. et al. Prioritizing hetero-metallic interfaces via thermodynamics inertia and kinetics zincophilia metrics for tough Zn-based aqueous batteries. *Adv. Mater.* **35**, 1–10 (2023).
46. Li, Q., Chen, A., Wang, D., Pei, Z. & Zhi, C. "Soft shorts" hidden in zinc metal anode research commentary. *Joule* **6**, 273–279 (2022).
47. Liang, G. et al. Gradient fluorinated alloy to enable highly reversible Zn-metal anode chemistry. *Energy Environ. Sci.* **15**, 1086–1096 (2022).
48. Kresse, G. & Furthmüller, J. Efficient iterative schemes for ab initio total-energy calculations using a plane-wave basis set. *Phys. Rev. B* **54**, 11169–11186 (1996).
49. Blöchl, P. E. Projector augmented-wave method. *Phys. Rev. B* **50**, 17953–17979 (1994).
50. Perdew, J. P., Burke, K. & Ernzerhof, M. Generalized gradient approximation made simple. *Phys. Rev. Lett.* **77**, 3865–3868 (1996).
51. Kelkkanen, A. K., Lundqvist, B. I. & Nørskov, J. K. Van der Waals effect in weak adsorption affecting trends in adsorption, reactivity, and the view of substrate nobility. *Phys. Rev. B* **83**, 1–4 (2011).
52. Henkelman, G., Uberuaga, B. P. & Jónsson, H. A climbing image nudged elastic band method for finding saddle points and minimum energy paths. *J. Chem. Phys.* **113**, 9901–9904 (2000).
53. Min, Z., Yang, C., Zhong, G. H. & Lu, Z. First-principles insights into lithium-rich ternary phosphide superionic conductors: solid electrolytes or active electrodes. *ACS Appl. Mater. Interfaces* **14**, 18373–18382 (2022).

Acknowledgements

This work was financed by Shenzhen Science and Technology Program (JCYJ20230807142508016) to G.L., Guangdong Basic and Applied Basic

Research Foundation (2024A1515010915 and 2024A1515010679) to G.L. and Y.S., Shenzhen Science and Technology Program (Grant No. RCBS20231211090650089) to G.L., State Key Laboratory of New Textile Materials and Advanced Processing Technologies (No. FZ20230010) to G.L. We gratefully acknowledge HZWTECH for providing computation facilities.

Author contributions

G.L., and Y.S. conceived and supervised the project. Y.H. and G.Z. prepared the materials. Y.H., Z.M., G.Z., Y.Z., Y.P., and C.C. conducted the characterization and analyzed the data. Z.M. performed density functional theory calculation. Y.H., G.L., Y.S., and H.C. wrote the paper, and all authors engaged in discussions related to the manuscript.

Competing interests

The authors declare no competing interests.

Additional information

Supplementary information The online version contains supplementary material available at https://doi.org/10.1038/s41467-025-58473-3.

Correspondence and requests for materials should be addressed to Yuanmiao Sun or Guojin Liang.

Peer review information *Nature Communications* thanks the anonymous, reviewers for their contribution to the peer review of this work. A peer review file is available.